METIS: TRAINING LLMS WITH FP4 QUANTIZATION

Anonymous authors
Paper under double-blind review

ABSTRACT

This work identifies anisotropy in the singular value spectra of parameters, activations, and gradients as the fundamental barrier to low-bit training of large language models (LLMs). These spectra are dominated by a small fraction of large singular values, inducing wide numerical ranges that cause quantization bias and severe spectral distortion, ultimately degrading training performance. This work presents *Metis*, a spectral-domain quantization framework that partitions anisotropic spectra into narrower sub-distributions for independent quantization, thereby reducing errors and preserving spectral structure. To minimize overhead, Metis leverages two key properties of the dominant spectral subspace: preservation via sparsely random sampling and preservation via random projection, reducing decomposition cost to a negligible level. On LLaMA-3 8B trained with 100B tokens, Metis enables robust W4A4G4 training with FP4 quantization of weights, activations, and gradients, yielding only a 0.4% training loss gap and a 0.1% degradation in downstream accuracy relative to BF16. Beyond matching BF16 fidelity, Metis also surpasses our implementation of Nvidia's recently announced (yet to be publicly released) FP4 recipe, consistently achieving lower loss and higher downstream accuracy while incurring significantly lower computational overhead. The code implementation for Metis is available at: `https://anonymous.4open.science/r/Metis-quantization-644B`.

1 INTRODUCTION

Training large language models (LLMs) with low-bit quantization of parameters, activations, and gradients offers substantial gains in efficiency, cost, and scalability. In recent years, progress has advanced from FP32 to BF16 and, more recently, to FP8 training (Micikevicius et al., 2022; Peng et al., 2023; Perez et al., 2023). Looking ahead, Nvidia's Blackwell technical report shows that the NVFP4 format reduces memory consumption by 1.8× and accelerates General Matrix Multiplications (GeMM) by 7× compared to FP8, underscoring the efficiency potential of FP4 training (Alvarez et al.; Devleker & Ghodsian). However, pushing the training frontier further down to FP4 is not a straightforward continuation: FP4 imposes exponentially tighter constraints on precision and dynamic range, which conflict with the inherently wide distributions of parameters, activations, and gradients.

This study investigates the origins of these wide distributions and analyzes their impact on training stability and effectiveness under FP4 quantization. The key findings are outlined below and visualized in Fig. 1.

Anisotropy is universal in modern LLMs. In weight, activation, and gradient matrices, a small fraction of singular values dominate, yielding a highly imbalanced spectrum. This phenomenon is consistently observed across model architectures and parameter scales up to 671B.

Anisotropy induces wide numerical distributions. Wide distributions of weights, activations, and gradients arise from the superposition of singular components: larger components contribute to the large-value region, whereas smaller ones concentrate near zero. This spread originates from variability in singular values, which projects aligned components into entries of corresponding magnitudes.

Quantization bias induces spectral distortion. Commonly used block-level low-bit quantization introduces bias that disproportionately favors large values, thereby reducing the effective resolution for small values. Under anisotropy, this effect leads to severe distortion in spectral space: smaller singular components incur substantially larger value errors and direction perturbations than their larger counterparts.

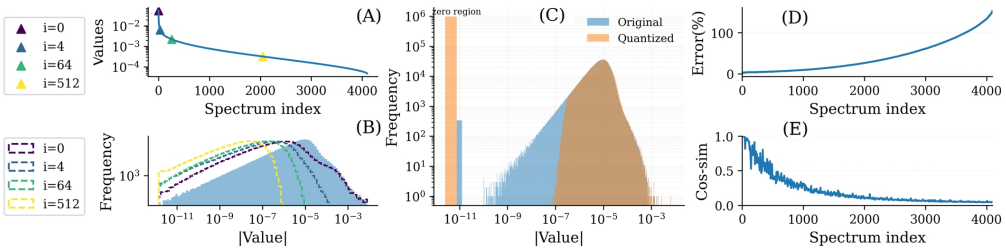

Figure 1: Overview of anisotropy and its impact on quantization, illustrated using a gradient matrix from LLaMA-3 8B. (A) Singular value spectrum exhibits strong anisotropy, with a few singular values dominating the spectrum. (B) The wide matrix distribution arises from the superposition of singular components: large components (e.g., i=0) drive the high-value region, while small components concentrate near zero. (C) Quantization bias disproportionately rounds many small values to zero. (D–E) In spectral space, smaller singular components incur substantially larger relative quantization errors in singular values and more severe perturbations in singular directions. Details corresponding to (A) in Section 2.1, (B) in Section 2.2, and (C–E) in Section 2.3.

Inspired by these findings, we propose *Metis*, a quantization framework that preserves the spectral structure under FP4 formats and allows robust FP4 training. Metis operates in the spectral domain, applying decomposition to weight, activation, and gradient matrices to disentangle dominant from long-tailed singular components, thereby allowing quantization over substantially narrower distributions. A central challenge is the computational complexity of spectral decomposition. To address this, we leverage two key structural properties revealed in our empirical study:

(i) *Subspace Preservation via Sparsely Random Sampling*, where the dominant subspace estimated from a sparsely random sampled subset is reliably generalized to the whole batch;

(ii) *Subspace Preservation via Random Projection*, where the dominant subspace can be faithfully captured within a reduced hidden dimension via random projection.

Building on these insights, Metis renders the decomposition cost negligible by employing sparse random sampling over sequences and random projections on the hidden dimension, each reducing complexity by approximately two orders of magnitude.

Metis enables robust W4A4G4 training by quantizing all GeMM matrices to 4-bit floating point. On an 8B LLaMA-3 model (et al., 2024) trained with 100B tokens from the DCLM dataset (Li et al., 2025), Metis narrows the gap to BF16 to only a 0.4% increase in training loss and a 0.1% degradation in downstream accuracy. Compared to our implementation of NVIDIA's recently announced (but not yet publicly released) FP4 recipe (Devleker & Ghodsian), Metis consistently achieves lower training loss and higher downstream accuracy while incurring significantly less computational overhead.

2 Analysis

Anisotropy emerges as a key structural factor underlying the wide distributions observed in weights, activations, and gradients. This section analyzes these anisotropic matrices and examines how they misalign with low-bit quantization schemes. Unless otherwise specified, all experiments are conducted on the LLaMA-3 8B model trained on 100B tokens from the DCLM dataset.

2.1 Anisotropy: A Universal Property of Modern LLMs

For a matrix $\mathbf{M} \in \mathbb{R}^{m\times n}$, we perform Singular Value Decomposition (SVD) to obtain singular values $\{\sigma_i\}_{i=1}^{\min(m,n)}$, left singular vectors $\{\mathbf{u}_i\} \in \mathbb{R}^m$, and right singular vectors $\{\mathbf{v}_i\} \in \mathbb{R}^n$, such that $\mathbf{M} = \sum_{i=1}^{\min(m,n)} \sigma_i \mathbf{u}_i \mathbf{v}_i^\top$. We assume singular values are sorted in descending order, i.e., $\sigma_1 \geq \sigma_2 \geq \cdots \geq \sigma_r > 0$ with $r = \min(m, n)$.

Anisotropy is characterized by a spectrum where a few leading singular values dominate, yielding a highly imbalanced distribution across directions. Previous studies have reported anisotropy in activation matrices (Ethayarajh, 2019; Mu et al., 2017; Puccetti et al., 2022; Rudman & Eickhoff,

2023; Yu et al., 2021), and our analysis further demonstrates that it is universal across weights, activations, and gradients. As shown in Figure 2 (A), their singular value spectra exhibit pronounced anisotropy, with only 0.63%, 3.15%, and 2.91% of components (identified by the elbow point of maximum curvature) dominating the spectra of weights, activations, and gradients, respectively. We further validate this pattern on publicly released models, including the Qwen family (Bai et al., 2023) and DeepSeek-R1 (Liu et al., 2024), where weight matrices from 7B to 671B parameters consistently show fewer than 3% of singular values dominating the spectrum, confirming anisotropy as a universal property across architectures and scales.

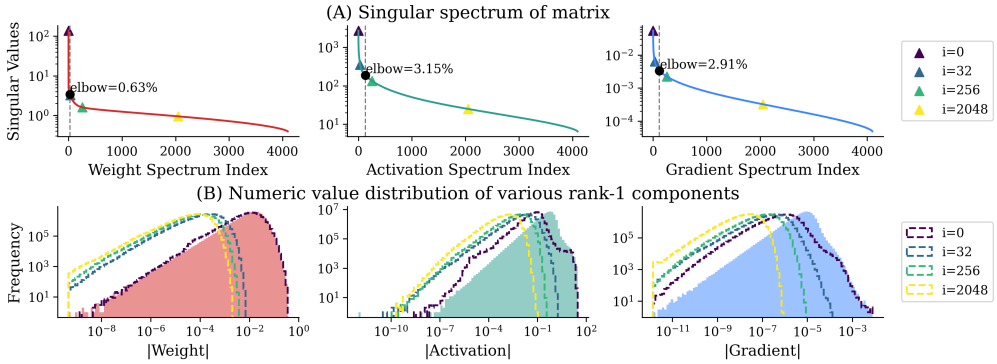

Figure 2: Analysis of weight, activation, and gradient matrices (layer 32, FeedForward(FFN)). (A) The singular value spectra exhibit strong anisotropy, with only 0.63%, 3.15%, and 2.91% of components (identified by the elbow point of maximum curvature) dominating the spectrum. (B) Filled regions denote full-matrix distributions; dashed histograms showes selected rank-1 components ($\mathbf{u}_i\sigma_i\mathbf{v}_i^\top$ for $i = 0, 16, 128, 1024$). Dominant components (e.g., $i = 0$) drive the high-value region, while smaller ones (e.g., $i = 1024$) contribute near zero. See A.1 for additional results.

2.2 Anisotropy Induces Wide Numerical Distributions

The wide distributions of weights, activations, and gradients arise from the superposition of singular components ($\mathbf{u}_i\sigma_i\mathbf{v}_i^\top$): dominant components (e.g., $i = 0$) account for the large-value region, whereas smaller components (e.g., $i = 1024$) concentrate near zero, as illustrated in Fig. 2 (B).

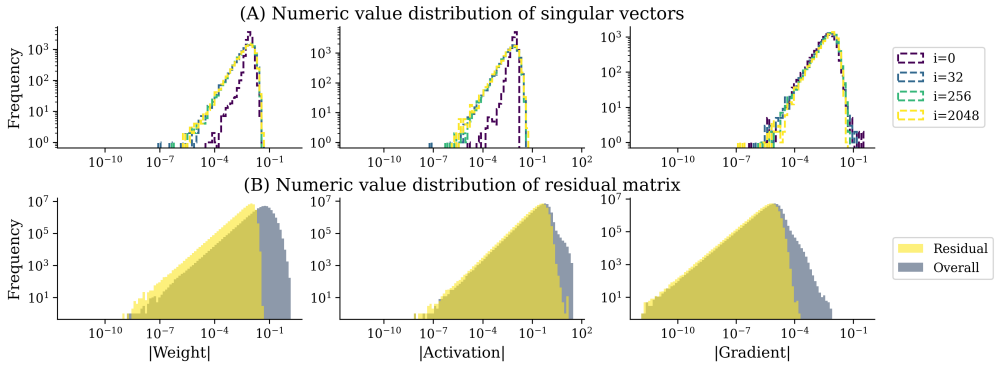

Figure 3: Analysis of weight, activation, and gradient matrices with hidden dimension 4096 (layer 32, FFN). (A) Left singular vector distributions: all exhibit similar shapes with widths much smaller than that of the full matrix. (B) Yellow regions show the residuals after removing the top 128 components ($3\% \times 4096 \approx 123$, rounded to the nearest power of two), while the grey region represents the original matrix distribution. The residuals are one to two orders of magnitude narrower than the full matrix, confirming that wide ranges originate from dominant components. More results in A.2

Wide distributions arise from the skewed singular value spectrum. This spread originates from variability in singular values, which project aligned components into entries of corresponding magnitudes. In the SVD decomposition $\mathbf{M} = \sum_i \sigma_i \mathbf{u}_i \mathbf{v}_i^\top$, large singular values amplify aligned components into high-magnitude entries, whereas small singular values suppress others toward near zero, thereby producing long-tailed distributions. After isolating the impact of singular values,

Fig. 3(A) shows that the singular vectors all exhibit similar shapes with widths far narrower than that of the full matrix. Thus, the wide ranges are a direct consequence of the skewed singular spectrum.

Residual singular components confirm the dominant subspace effect. To validate this mechanism, we analyze residual matrices, corresponding to the long-tail singular components, after subtracting the leading singular components amplified by large singular values. As shown in Fig. 3 (B), removing the top 3% of components, which dominate the spectrum, yields residual distributions one to two orders of magnitude narrower than those of the full matrix. This demonstrates that wide ranges arise primarily from the dominant subspace, while the residual remains quantization-friendly.

2.3 Quantization Bias: Spectral Distortion

In extreme low-bit regimes such as FP4, block-wise quantization is a commonly-used approach. By restricting scaling to small blocks with fewer entries, the likelihood of encountering extreme values is reduced, resulting in narrower local distributions and finer-grained scaling that mitigates quantization error (Rouhani et al., 2023; Nvidia, 2025). Formally, a b-bit quantizer $\mathcal{Q}_b$ maps a matrix $\mathbf{M} \in \mathbb{R}^{m\times n}$ to its quantized form $\overline{\mathbf{M}} = \mathcal{Q}_b(\mathbf{M})$. Throughout the paper, we will use the bar symbol to denote the matrix after quantization for simplicity. The matrix is partitioned into fixed-size blocks (e.g., size 16 in the NVFP4 format (Nvidia, 2025)). For each block $\mathbf{E} \in \mathbb{R}^t$, NVFP4 selects a single scaling factor s in FP8 (E4M3), set by the block's maximum magnitude and rounded up to the nearest representable FP8 value to ensure coverage. Each element is then quantized as $\mathcal{Q}_4^{\mathrm{NV}}(\mathbf{e}_i) = \mathrm{round}\big(\frac{\mathbf{e}_i}{s}\big) \cdot s$.

Quantization bias. In broad distributions, where the range can span multiple orders of magnitude, as observed in weight, activation, and gradient matrices in Fig. 2, determining the scaling factor s by the block maximum introduces bias. This bias disproportionately favors large values while suppressing the resolution available for small ones. As shown in Fig. 1 (C), nearly half of the values are rounded entirely to zero after quantization, resulting in the destructive loss of the information they represent.

Spectral distortion. In an anisotropic matrix with uneven singular value distribution, quantization bias causes severe distortion in spectral space, especially for small singular components. As shown in Fig. 1 (D) (E), all components suffer relative errors in singular values and directional perturbations, with smaller ones exhibiting greater distortion in both magnitude and direction.

3 Metis

We propose *Metis*, an FP4 training framework designed to address the challenge of spectral anisotropy. Metis partitions the spectrum into narrower sub-distributions and applies quantization independently within each. This design yields two benefits: (i) as shown in Fig. 3, each sub-distribution is significantly narrower than the full spectrum, reducing quantization error; and (ii) it prevents small singular components from being overwhelmed by large ones, thereby mitigating perturbations in singular values and preserving directional consistency within the subspace.

The central challenge, however, lies in the high cost of repeatedly performing spectral decomposition during training. Section 3.1 shows that anisotropy induces two key properties of the dominant subspace, preservation via sparsely random sampling and random projection, making scalable spectral decomposition feasible. Section 3.2 integrates this scalable decomposition into GeMM, the source of over 95% of the training workload in large language models (Vaswani et al., 2017; Wang et al., 2025), applying FP4 quantization to all GeMMs in both forward and backward passes. Section 3.3 analyzes the additional computational complexity introduced by Metis.

3.1 Enabling Properties for Scalable Spectral Decomposition

The prohibitive cost of spectral decomposition presents a major obstacle to deploying spectral-domain quantization at scale. Let $\mathbf{X} \in \mathbb{R}^{l\times m}$ denote the activation tensor, where $l = b \cdot s$ with b the batch size, s the sequence length, and m the hidden dimension. In practice, l can reach millions while m is typically in the thousands. Performing a full SVD on such matrices at every iteration incurs a cost of $\mathcal{O}(lm^2)$, making direct application impractical.

However, anisotropy offers a crucial opportunity: it causes a small number of singular values k to dominate, with $k \ll l, m$, so spectral decomposition only needs to isolate the corresponding

dominant subspace, yielding markedly narrower spectral sub-distributions. Building on this, our further investigation reveals two properties that enable dimension reduction along both the sequence and hidden axes: (i) the dominant subspace estimated from a sparsely sampled subset generalizes reliably to the full batch, and (ii) the dominant subspace can be faithfully captured within a reduced hidden dimension via random projection.

Subspace Preservation via Sparsely Random Sampling. The sequence dimension l is typically orders of magnitude larger than the dominant subspace dimension k. Intuitively, this abundance of samples ensures that the dominant subspace can be estimated stably even from a small random subset of samples. From a theoretical perspective, the anisotropic structure guarantees that random subsampling preserves the dominant subspace with high probability. Let $\Sigma = \frac{1}{l}\mathbf{X}^\top\mathbf{X} \in \mathbb{R}^{m\times m}$ be the covariance. For a random subset $\mathbf{X}_\Omega \in \mathbb{R}^{l_k\times n}$ with $l_k \ll l$, the sample covariance $\hat{\mathbf{\Sigma}} = \frac{1}{l_k}\mathbf{X}_\Omega^\top\mathbf{X}_\Omega$ satisfies the matrix Chernoff (Tropp, 2012):

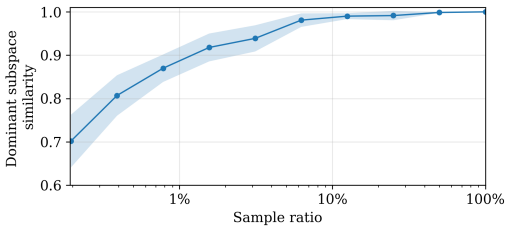

Figure 4: Subspace alignment between the dominant subspace of the full batch and that of randomly sampled subsets of sequences. Alignment quickly saturates as the sample ratio increases, with just 1% of sequences achieving nearly 0.9 alignment with the full-batch subspace. More results in B.1.

$$\Pr\Big[\|\hat{\mathbf{\Sigma}} - \mathbf{\Sigma}\|_2 \le \epsilon\|\mathbf{\Sigma}\|_2\Big] \ge 1-\delta, \text{whenever } l_k = \mathcal{O}\Big(\frac{n}{\epsilon^2}\log\frac{n}{\delta}\Big).$$

Combined with the Davis–Kahan theorem (Davis & Kahan, 1970), $\|\mathbf{A}_k\mathbf{A}_k^\top - \hat{\mathbf{A}}_k\hat{\mathbf{A}}_k^\top\|_2 \le \frac{\|\hat{\mathbf{\Sigma}}-\mathbf{\Sigma}\|_2}{\Delta}$, where $\mathbf{A}_k$ and $\hat{\mathbf{A}}_k \in \mathbb{R}^{m\times k}$ are the top-k eigenspaces of $\mathbf{\Sigma}$ and $\hat{\mathbf{\Sigma}}$, and Δ is the eigengap, this guarantees that the dominant subspace estimated from a small random subset faithfully recovers that of the full batch. Empirically, we measure the alignment of the dominant subspace between the full batch and randomly sampled subsets using the mean squared canonical correlation between their orthonormal bases. We observe rapid saturation as the sample ratio increases. For instance, as shown in Fig. 4, sampling only 1% of sequences achieves nearly 0.9 overlap with the full-batch subspace, demonstrating the effectiveness of this subspace approximation.

Subspace Preservation via Random Projection. We further establish that the dominant spectral structure remains stable under random projections of the hidden dimension. Let $\mathbf{\Omega} \in \mathbb{R}^{n\times(k+s)}$ be a Gaussian test matrix with oversampling parameter s, and form the sketch $\mathbf{Z} = \mathbf{X}\mathbf{\Omega}$ with thin QR factorization $\mathbf{Z} = \mathbf{H}\mathbf{R}$. Randomized SVD theory (Halko et al., 2011) shows that, with high probability, the projection error $\|(\mathbf{I} - \mathbf{H}\mathbf{H}^\top)\mathbf{X}\|_2$ is controlled by the tail singular values of $\mathbf{X}$. Furthermore, by Davis–Kahan, the subspace error for the top-k eigenspace satisfies $\|\mathbf{A}_k\mathbf{A}_k^\top - (\mathbf{H}\tilde{\mathbf{A}}_k)(\mathbf{H}\tilde{\mathbf{A}}_k)^\top\|_2 \le \frac{2\|(\mathbf{I}-\mathbf{H}\mathbf{H}^\top)\mathbf{X}\|_2}{\Delta}$, where $\tilde{\mathbf{A}}_k \in \mathbb{R}^{m\times k}$ are the top-k eigenspaces of $\mathbf{H}^\top\mathbf{\Sigma}\mathbf{H}$. This demonstrates that a modest oversampling parameter s and a nontrivial spectral gap suffice to ensure that Gaussian projections preserve the dominant subspace with high fidelity, enabling accurate recovery without operating in the full ambient dimension m.

Scalable Spectral Decomposition. Leveraging these properties, we adopt a two-step procedure for efficient decomposition. First, *sparse random sampling* selects less than 1% of sequences to estimate the dominant subspace, which is then broadcast to the full batch. Second, we apply *randomized SVD* to recover the top-k components. This reduces the complexity from $\mathcal{O}(ln^2)$ to $\mathcal{O}(l_knk)$, while the additional cost remains asymptotically negligible compared with forward and backward GeMM.

3.2 Spectral Decomposition

Each matrix in GeMM is decomposed into a low-rank component and a residual: low-rank singular values are kept in high precision, while the associated singular vectors and residual are quantized to low bit. Metis handles parameters, activations, and gradients differently: for parameters, low-rank and residual parts are stored as separate trainable variables and updated independently; for activations and gradients, spectral decompositions are recomputed dynamically at each iteration.

Forward pass. Let $\mathbf{W} \in \mathbb{R}^{m\times n}$ denote a weight matrix and $\mathcal{X} \in \mathbb{R}^{b\times s\times m}$ an input activation tensor, where b is the batch size, s the sequence length, and m the hidden dimension. For the GeMM

operation, $\mathbf{X}$ is reshaped into a matrix of size $\mathbf{X} \in \mathbb{R}^{l\times m}$ with $l = b \cdot s$, yielding $\mathbf{Y} = \mathbf{X}\mathbf{W} \in \mathbb{R}^{l\times n}$. Our goal is to quantize this GeMM computation under low-bit formats.

A rank-k approximation of $\mathbf{W}$ is given by $\hat{\mathbf{W}}_k = \mathbf{U}_k\mathbf{S}_k\mathbf{V}_k^\top$, where $\mathbf{U}_k \in \mathbb{R}^{m\times k}$, $\mathbf{V}_k \in \mathbb{R}^{n\times k}$, and $\mathbf{S}_k = \mathrm{diag}(\sigma_1, \ldots, \sigma_k) \in \mathbb{R}^{k\times k}$. The residual is $\mathbf{W}_\mathrm{R} = \mathbf{W} - \hat{\mathbf{W}}_k$, so that $\mathbf{W} = \hat{\mathbf{W}}_k + \mathbf{W}_\mathrm{R} = \mathbf{U}_k\mathbf{S}_k\mathbf{V}_k^\top + \mathbf{W}_\mathrm{R}$. Similarly, the activation matrix $\mathbf{X}$ is decomposed as: $\mathbf{X} = \hat{\mathbf{X}}_k + \mathbf{X}_\mathrm{R} = \mathbf{A}_k\mathbf{\Lambda}_k\mathbf{B}_k^\top + \mathbf{X}_\mathrm{R}$, where $\mathbf{A}_k \in \mathbb{R}^{l\times k}$, $\mathbf{B}_k \in \mathbb{R}^{m\times k}$ and $\mathbf{\Lambda}_k \in \mathbb{R}^{k\times k}$.

Accordingly, the forward GeMM can be written as

$$\mathbf{Y} = (\mathbf{A}_k\mathbf{\Lambda}_k\mathbf{B}_k^\top + \mathbf{X}_\mathrm{R})(\mathbf{U}_k\mathbf{S}_k\mathbf{V}_k^\top + \mathbf{W}_\mathrm{R}) \tag{1}$$

The quantization function $\mathcal{Q}_b$ is then applied separately to matrices in Eq. 1 other than $\mathbf{S}_k$ and $\mathbf{\Lambda}_k$. Specifically, the forward computation of $\mathbf{Y}$ under b-bit quantization, denoted as $\hat{\mathbf{Y}}$, is computed as

$$\begin{aligned}\hat{\mathbf{Y}} &= (\mathcal{Q}_b(\mathbf{A}_k)\mathbf{\Lambda}_k\mathcal{Q}_b(\mathbf{B}_k^\top) + \mathcal{Q}_b(\mathbf{X}_\mathrm{R}))(\mathcal{Q}_b(\mathbf{U}_k)\mathbf{S}_k\mathcal{Q}_b(\mathbf{V}_k^\top) + \mathcal{Q}_b(\mathbf{W}_\mathrm{R})) \\ &= \overline{\mathbf{X}}\overline{\mathbf{U}}_k\mathbf{S}_k\overline{\mathbf{V}}_k^\top + \overline{\mathbf{X}}\overline{\mathbf{W}}_\mathrm{R}.\end{aligned} \tag{2}$$

Backward pass. In backward propagation, we quantize the GeMM operations associated with derivative computations of matrices in Eq. 1. Formally, denote the derivatives of the loss function $\mathcal{L}$ with respect to (w.r.t) $\mathbf{Y}$ as $\mathbf{D} = \frac{\partial\mathcal{L}}{\partial\mathbf{Y}} \in \mathbb{R}^{l\times n}$, we need to compute the following derivatives for updating parameters: $\frac{\partial\mathcal{L}}{\partial\mathbf{X}}$, $\frac{\partial\mathcal{L}}{\partial\mathbf{U}_k}$, $\frac{\partial\mathcal{L}}{\partial\mathbf{S}_k}$, $\frac{\partial\mathcal{L}}{\partial\mathbf{V}_k}$, and $\frac{\partial\mathcal{L}}{\partial\mathbf{W}_\mathrm{R}}$. Similarly, we first decompose $\mathbf{D}$ into a SVD low-rank approximation and the residual, which is $\mathbf{D} = \mathbf{P}_k\mathbf{T}_k\mathbf{Q}_k^\top + \mathbf{D}_\mathrm{R}$, where $\mathbf{P}_k \in \mathbb{R}^{l\times k}$, $\mathbf{Q}_k \in \mathbb{R}^{n\times k}$, $\mathbf{T}_k \in \mathbb{R}^{k\times k}$. The derivative $\frac{\partial\mathcal{L}}{\partial\mathbf{X}}$ is computed as

$$\begin{aligned}\frac{\partial\mathcal{L}}{\partial\mathbf{X}} = \frac{\partial\mathcal{L}}{\partial\mathbf{Y}}\frac{\partial\mathbf{Y}}{\partial\mathbf{X}} &= \mathbf{D}(\mathbf{V}_k\mathbf{S}_k^\top\mathbf{U}_k^\top + \mathbf{W}_\mathrm{R}^\top), \\ &= \mathbf{P}_k\mathbf{T}_k\mathbf{Q}_k^\top\mathbf{V}_k\mathbf{S}_k^\top\mathbf{U}_k^\top + \mathbf{P}_k\mathbf{T}_k\mathbf{Q}_k^\top\mathbf{W}_\mathrm{R}^\top + \mathbf{D}_\mathrm{R}\mathbf{V}_k\mathbf{S}_k^\top\mathbf{U}_k^\top + \mathbf{D}_\mathrm{R}\mathbf{W}_\mathrm{R}^\top.\end{aligned}$$

We then compute $\frac{\partial\mathcal{L}}{\partial\mathbf{X}}$ under 4-bit quantization as

$$\hat{\frac{\partial\mathcal{L}}{\partial\mathbf{X}}} = \overline{\mathbf{P}}_k\mathbf{T}_k\overline{\mathbf{Q}}_k^\top\overline{\mathbf{V}}_k\mathbf{S}_k^\top\overline{\mathbf{U}}_k^\top + \overline{\mathbf{P}}_k\mathbf{T}_k\overline{\mathbf{Q}}_k^\top\overline{\mathbf{W}}_\mathrm{R}^\top + \overline{\mathbf{D}}_\mathrm{R}\overline{\mathbf{V}}_k\mathbf{S}_k^\top\overline{\mathbf{U}}_k^\top + \overline{\mathbf{D}}_\mathrm{R}\overline{\mathbf{W}}_\mathrm{R}^\top. \tag{3}$$

Following a similar pathway, we compute other derivatives under 4-bit quantization as follows:

$$\hat{\frac{\partial\mathcal{L}}{\partial\mathbf{U}_k}} = \overline{\mathbf{X}}^\top\overline{\mathbf{P}}_k\mathbf{T}_k\overline{\mathbf{Q}}_k^\top\overline{\mathbf{V}}_k\overline{\mathbf{S}}_k^\top + \overline{\mathbf{X}}^\top\overline{\mathbf{D}}_\mathrm{R}\overline{\mathbf{V}}_k\overline{\mathbf{S}}_k^\top, \hat{\frac{\partial\mathcal{L}}{\partial\mathbf{S}_k}} = \overline{\mathbf{U}}_k^\top\overline{\mathbf{X}}^\top\overline{\mathbf{P}}_k\mathbf{T}_k\overline{\mathbf{Q}}_k^\top\overline{\mathbf{V}}_k + \overline{\mathbf{U}}_k^\top\overline{\mathbf{X}}^\top\overline{\mathbf{D}}_\mathrm{R}\overline{\mathbf{V}}_k,$$
$$\hat{\frac{\partial\mathcal{L}}{\partial\mathbf{V}_k}} = \overline{\mathbf{S}}_k^\top\overline{\mathbf{U}}_k^\top\overline{\mathbf{X}}^\top\overline{\mathbf{P}}_k\mathbf{T}_k\overline{\mathbf{Q}}_k^\top + \overline{\mathbf{S}}_k^\top\overline{\mathbf{U}}_k^\top\overline{\mathbf{X}}^\top\overline{\mathbf{D}}_\mathrm{R}, \hat{\frac{\partial\mathcal{L}}{\partial\mathbf{W}_\mathrm{R}}} = \overline{\mathbf{X}}^\top\overline{\mathbf{P}}_k\mathbf{T}_k\overline{\mathbf{Q}}_k^\top + \overline{\mathbf{X}}^\top\overline{\mathbf{D}}_\mathrm{R}.$$

3.3 Discussion on Training efficiency

Since Nvidia's Blackwell FP4 training stack is not yet publicly available, native NVFP4 training is unavailable. Thus, we emulate NVFP4 in BF16, as shown in C.1. Consequently, the actual runtime speedup and memory savings of FP4 training cannot be directly measured. We therefore analyze Metis's additional computational overhead, arising from (i) the extra small-scale GeMMs introduced by the decomposition and (ii) the decomposition itself.

Forward pass. In the baseline, evaluating $\mathbf{Y} = \mathbf{X}\mathbf{W}$ requires $\mathcal{O}(lmn)$ operations. Under Metis, the forward computation follows Eq. 1, where the additional mixed products introduce $\mathcal{O}(lmk + mnk + lnk)$ overhead on top of the baseline cost. Moreover, the activation decomposition performed at each step adds $\mathcal{O}(l_k mk)$, where $l_k \ll l$ by sparse random sampling.

Backward pass. In the baseline, gradients with respect to $\mathbf{X}$ and $\mathbf{W}$ require $\mathcal{O}(lmn)$ operations. Under Metis, gradient computation follows Eq. 3, where mixed products contribute $\mathcal{O}(lmk + mnk + lnk)$. In addition, output gradient decomposition at each step adds $\mathcal{O}(l_k nk)$.

Overall complexity. Combining forward and backward contributions, Metis introduces an additional cost of $\mathcal{O}(lmk + mnk + lnk + l_k mk + l_k nk)$ per training step, which is asymptotically much smaller than the baseline $\mathcal{O}(lmn)$, making Metis tractable at the scale of modern LLMs.

4 EXPERIMENTS

This section evaluates Metis on training loss and downstream task accuracy.

Models and Datasets. We conduct experiments on GPT-2 (130M and 1.1B) (Radford et al., 2019) and LLaMA-3 (8B) (et al., 2024). For pretraining, we use the DCLM (Li et al., 2025) dataset and train each model on 100B tokens. The raw data are segmented to split long documents and concatenate short ones, filtered to remove non-Unicode and non-English content, and further processed with Qwen3 to discard entries whose perplexity deviates by more than two standard deviations from the mean. For downstream evaluation, we consider three task types: question answering, classification, and cloze prediction. For question answering, we use ARC (Clark et al., 2018), RACE (Lai et al., 2017), and BoolQ (Clark et al., 2019); for classification, we use HellaSwag (Zellers et al., 2019) and PIQA (Bisk et al., 2019); and for cloze prediction, we use LAMBADA (OpenAI) (Kazemi et al., 2023).

FP4 Training. The efficacy of Metis under FP4 quantization is evaluated against both FP4 and BF16 baselines. All FP4 training in this work adopts W4A4G4 quantization, where weights, activations, and gradients are represented in the E2M1 NVFP4 format. Due to NVIDIA's closed-source FP4 training software stack, native hardware-supported FP4 training is not currently accessible; consequently, our experiments with NVFP4 are conducted through simulation in BF16. Stochastic rounding (SR) is applied by default in all FP4 experiments, as it mitigates quantization bias, is orthogonal to other methods. The Metis rank is fixed at 1.5% for low-rank approximation in both forward and backward passes, as our sensitivity analysis in C.2 shows that 1.5% is sufficient to maintain performance.

4.1 MAIN RESULTS

Training Loss. Fig. 5 shows the training loss curves of the BF16 baseline, NVFP4, and NVFP4 + Metis, while Table 1 reports the corresponding final test losses. NVFP4 exhibits a clear gap relative to the BF16 baseline, particularly on LLaMA-3 8B, with test loss increasing by 3–4% across all models. In contrast, Metis narrows the gap to 0.4% on LLaMA-3 8B and even achieves slightly lower loss than the BF16 baseline on GPT-2 models.This expressivity enhancement of Metis over the BF16 baseline may stem from the separation of low-rank and residual branches of weight matrices during training, which reduces interference between feature subspaces and contributes to the observed performance gains. We further examine the spectrum of the residual matrix to test whether anisotropy re-emerges. The results in C.3 show it does not: the singular value spectrum of the residual matrix remains flat, indicating that anisotropy is effectively addressed by the low-rank branch.

Performance on Downstream Tasks. As shown in Table 1, direct NVFP4 quantization results in an average drop of 1% relative to the BF16 baselines across all models. In contrast, Metis consistently outperforms these FP4 baselines, reducing the drop to 0.1% on LLaMA-3 8B and even slightly surpassing the BF16 baseline on GPT-2 models. These findings are consistent with the loss results reported earlier and demonstrate Metis's ability not only to preserve but, in some cases, to enhance model expressiveness under ultra-low-bit constraints.

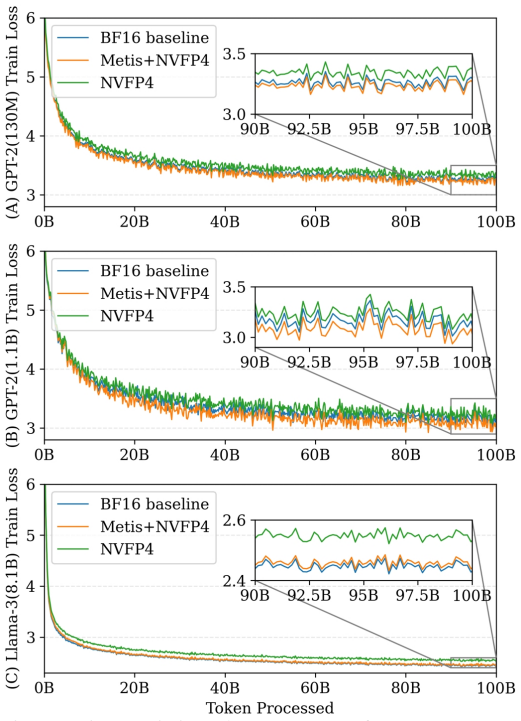

Figure 5: Training loss curves for (A) GPT-2 130M, (B) GPT-2 1.1B, and (C) LLaMA-3 8B. Direct NVFP4 incurs a loss gap of 3–4% relative to BF16 baseline, while Metis reduces the gap to 0.4% on LLaMA-3 and even slightly surpasses the BF16 baseline on GPT-2 models. This may be attributed to the separation of low-rank and residual branches in weight matrices, which reduces interference between feature subspaces.

Table 1: Downstream performance across different settings, reported with task-specific metrics. Direct NVFP4 quantization leads to an average drop of 1% relative to the BF16 baseline, while Metis reduces the gap to 0.1% on LLaMA-3 and slightly surpasses BF16 on GPT-2 models.

Model	Method	Loss	ARC-C	ARC-E	BoolQ	LAMBADA	PIQA	RACE	HellaSwag	Avg
GPT-2	BF16	3.23	**24.3**	**32.1**	60.4	31.3	**62.1**	47.3	**32.5**	41.4
(130M)	FP4	3.32	22.9	31.5	**60.7**	31.2	60.9	47.0	31.7	40.8
	FP4-Metis	**3.20**	24.1	31.9	60.2	**31.8**	61.8	**48.4**	32.2	**41.5**
GPT-2	BF16	3.09	**30.7**	59.5	**60.0**	35.4	**64.9**	47.3	41.1	48.4
(1.1B)	FP4	3.22	29.8	57.6	59.8	35.5	63.6	46.8	39.5	47.5
	FP4-Metis	**3.01**	30.1	**60.0**	59.5	**36.2**	64.1	**48.5**	**41.9**	**48.6**
LlaMa-3	BF16	**2.44**	32.4	**60.4**	59.2	**37.6**	70.5	**47.0**	**50.9**	**51.1**
(8B)	FP4	2.53	31.3	58.5	58.2	36.5	69.8	46.9	49.4	50.0
	FP4-Metis	2.45	**32.7**	59.6	**59.8**	37.0	**70.9**	46.5	50.7	51.0

4.2 Ablation Study

We ablate the two key components of Metis: Spectral Decomposition and Sparse Random Sampling.

Spectral Decomposition. To assess the role of spectral decomposition in weights, activations, and gradients, we replace it with direct FP4 quantization for each case. As shown in Table 2, removing spectral decomposition from gradients yields the largest degradation relative to Metis, with training loss increasing by 2.4% and downstream performance dropping by an average of 1.0%. In comparison, removing it from activations or weights results in smaller and similar degradations: training loss rises by about 0.5% and downstream performance decreases by an average of 0.3%.

Sparse Random Sampling. We further evaluate Sparse Random Sampling by replacing it with full-batch spectral decomposition. As shown in Table 2, sparse random sampling reduces the decomposition cost by orders of magnitude while introducing negligible performance impact.

Table 2: Performance of LLaMA-3 8B under different ablation settings of Metis. "w/o" denotes removal of the corresponding component. For FP4 training, spectral decomposition is most critical for gradients (removal yields the largest performance loss), followed by activations and weights. Sparse random sampling performs on par with full-batch spectral decomposition.

Method	Loss	ARC-C	ARC-E	BoolQ	LAMBADA	PIQA	RACE	HellaSwag	Avg
Metis	2.45	32.4	**60.4**	**59.2**	37.6	70.5	**47.0**	50.9	**51.1**
w/o Weight Decomposition	2.47	32.7	58.6	58.5	36.9	71.0	45.8	**51.4**	50.7
w/o Activation Decomposition	2.46	**33.9**	59.2	58.7	35.8	**71.6**	46.2	51.2	50.9
w/o Gradient Decomposition	2.51	30.6	60.3	59.1	36.2	68.5	46.8	49.7	50.1
w/o Sparse Random Sampling	**2.44**	32.9	60.0	59.1	**37.8**	70.7	46.7	50.5	**51.1**

4.3 Extended Evaluation

Comparison with Nvidia's Recipe. We compare Metis with Nvidia's recently announced (yet to be publicly released) FP4 recipe (Devleker & Ghodsian), which incorporates a random Hadamard transform alongside SR to mitigate the impact of outliers. Our implementation of this recipe is described in Appendix C.1. As shown in Table 3 for GPT-2 models, Nvidia's recipe results in 1-2% higher test loss and an average 0.5% drop in downstream performance relative to the BF16 baselines, whereas Metis surpasses BF16 on both test loss and average downstream performance.

Table 3: Nvidia's recipe yields 1-2% higher test loss and a 0.5% drop in downstream performance relative to BF16, whereas Metis surpasses BF16 on both metrics.

Model	Method	Loss	ARC-C	ARC-E	BoolQ	LAMBADA	PIQA	RACE	HellaSwag	Avg
GPT-2	BF16	3.23	**24.3**	**32.1**	**60.4**	31.3	**62.1**	47.3	**32.5**	41.4
(130M)	FP4-Metis	**3.20**	24.1	31.9	60.2	**31.8**	61.8	**48.4**	32.2	**41.5**
	FP4-Nvidia's Recipe	3.27	23.7	31.2	59.4	30.5	62.0	47.6	31.9	40.9
GPT-2	BF16	3.09	**30.7**	59.5	**60.0**	35.4	**64.9**	47.3	41.1	48.4
(1.1B)	FP4-Metis	**3.01**	30.1	**60.0**	59.5	36.2	64.1	**48.5**	**41.9**	**48.6**
	FP4-Nvidia's Recipe	3.15	28.6	59.8	59.3	**36.7**	63.2	48.0	40.2	47.9

The advantage of Metis lies in two aspects: (i) as shown in A.3, spectral decomposition yields much narrower residual distributions, whereas random Hadamard transform only smooths a few outliers without reducing overall spread; and (ii) as shown in Fig. 6, Metis attains better alignment of singular directions and lower singular-value error than both direct NVFP4 and NVFP4 with Nvidia's recipe, thereby preserving the spectral structure critical for model performance.

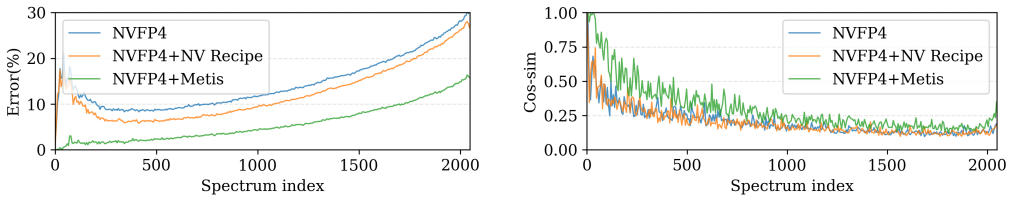

(a) (b)

Figure 6: Spectral preservation under different quantization strategies. (a) Alignment of left singular vectors measured by cosine similarity. (b) Relative error in singular values. Metis achieves the highest vector alignment and the lowest singular-value error relative to the BF16 baseline.

5 Related Works

Block-wise microscaling alleviates FP4's range mismatch but still compresses small values into few bins, causing information loss. Existing methods fall into three categories:

Channel-wise Re-parameterization. SmoothQuant (Xiao et al., 2023) applies calibrated per-channel scaling folded offline, Outlier Suppression+ (Wei et al., 2023) augments scaling with per-channel shifts, and OmniQuant (Shao et al., 2023) introduces learnable transforms with weight clipping. These diagonal methods still struggle with residual extremes in low-bit regimes.

Hadamard transformations. Orthogonal Hadamard rotations (Suresh et al., 2017) redistribute outliers across channels to relax per-block ranges. QuaRot (Ashkboos et al., 2024) applies them to hidden states and weights for end-to-end 4-bit inference, while QuIP (Chee et al., 2023) uses randomized preprocessing for weight-only 4-bit PTQ. HALO (Ashkboos et al., 2025) inserts rotations in both forward and backward passes to stabilize low-precision training. NVIDIA's FP4 recipe (Devleker & Ghodsian) similarly combines random Hadamard transforms with stochastic rounding for W4A4G4 training. Despite these advances, all Hadamard-based methods incur notable overhead from repeated rotations and mainly smooth outliers without narrowing overall distributions, leaving quantized tensors vulnerable to precision loss.

Outlier Separation. These methods divert extreme values into a small high-precision branch. Outlier Clamping and Compensation (Wang et al., 2025) clamps top-quantile activations and recovers clipped residuals via sparse GEMM, while SVDQuant (Li et al., 2024) shifts activation mass into weights and absorbs outlier energy in a high-precision low-rank branch. Both reduce error but rely on auxiliary precision paths, deviating from full FP4.

6 Conclusions

We identified anisotropy in the singular value spectra of parameters, activations, and gradients as a fundamental obstacle to low-bit LLM training and introduced *Metis*, a spectral-domain quantization framework that mitigates this challenge by partitioning spectra into narrower sub-distributions and preserving structural fidelity with negligible overhead. On LLaMA-3 8B, Metis enables robust W4A4G4 training with less than 0.4% loss gap and under 0.1% downstream degradation relative to BF16, while also surpassing Nvidia's FP4 recipe. These results establish Metis as a practical, high-fidelity approach for efficient FP4 training of large language models.

Limitations. Due to NVIDIA's closed-source FP4 training software stack and recipe, our experiments with NVFP4 are currently simulated in BF16 rather than executed with native hardware support; the recipe is implemented based on their technical report. We plan to validate the results once the official implementation becomes accessible.

REFERENCES

Eduardo Alvarez, Omri Almog, Eric Chung, Simon Layton, Dusan Stosic, Ronny Krashinsky, and Kyle Aubrey. Introducing nvfp4 for efficient and accurate low-precision inference. URL https://developer.nvidia.com/blog/introducing-nvfp4-for-efficient-and-accurate-low-precision-inference/.

Saleh Ashkboos, Amirkeivan Mohtashami, Maximilian L Croci, Bo Li, Pashmina Cameron, Martin Jaggi, Dan Alistarh, Torsten Hoefler, and James Hensman. Quarot: Outlier-free 4-bit inference in rotated llms. *Advances in Neural Information Processing Systems*, 37:100213–100240, 2024.

Saleh Ashkboos, Mahdi Nikdan, Soroush Tabesh, Roberto L Castro, Torsten Hoefler, and Dan Alistarh. Halo: Hadamard-assisted lower-precision optimization for llms. *arXiv preprint arXiv:2501.02625*, 2025.

Jinze Bai, Shuai Bai, Yunfei Chu, Zeyu Cui, Kai Dang, Xiaodong Deng, Yang Fan, Wenbin Ge, Yu Han, Fei Huang, et al. Qwen technical report. *arXiv preprint arXiv:2309.16609*, 2023.

Yonatan Bisk, Rowan Zellers, Ronan Le Bras, Jianfeng Gao, and Yejin Choi. Piqa: Reasoning about physical commonsense in natural language, 2019. URL https://arxiv.org/abs/1911.11641.

Jerry Chee, Yaohui Cai, Volodymyr Kuleshov, and Christopher M De Sa. Quip: 2-bit quantization of large language models with guarantees. *Advances in Neural Information Processing Systems*, 36: 4396–4429, 2023.

Christopher Clark, Kenton Lee, Ming-Wei Chang, Tom Kwiatkowski, Michael Collins, and Kristina Toutanova. Boolq: Exploring the surprising difficulty of natural yes/no questions, 2019. URL https://arxiv.org/abs/1905.10044.

Peter Clark, Isaac Cowhey, Oren Etzioni, Tushar Khot, Ashish Sabharwal, Carissa Schoenick, and Oyvind Tafjord. Think you have solved question answering? try arc, the ai2 reasoning challenge, 2018. URL https://arxiv.org/abs/1803.05457.

Chandler Davis and William Morton Kahan. The rotation of eigenvectors by a perturbation. iii. *SIAM Journal on Numerical Analysis*, 7(1):1–46, 1970.

Kirthi Devleker and Farshad Ghodsian. Nvfp4 trains with precision of 16-bit and speed and efficiency of 4-bit. URL https://developer.nvidia.com/blog/nvfp4-trains-with-precision-of-16-bit-and-speed-and-efficiency-of-4-bit/.

A. Grattafiori et al. The llama 3 herd of models. 2024.

Kawin Ethayarajh. How contextual are contextualized word representations? comparing the geometry of bert, elmo, and gpt-2 embeddings. *arXiv preprint arXiv:1909.00512*, 2019.

Nathan Halko, Per-Gunnar Martinsson, and Joel A Tropp. Finding structure with randomness: Probabilistic algorithms for constructing approximate matrix decompositions. *SIAM review*, 53(2): 217–288, 2011.

Mehran Kazemi, Najoung Kim, Deepti Bhatia, Xin Xu, and Deepak Ramachandran. Lambada: Backward chaining for automated reasoning in natural language, 2023. URL https://arxiv.org/abs/2212.13894.

Guokun Lai, Qizhe Xie, Hanxiao Liu, Yiming Yang, and Eduard Hovy. Race: Large-scale reading comprehension dataset from examinations, 2017. URL https://arxiv.org/abs/1704.04683.

Jeffrey Li, Alex Fang, Georgios Smyrnis, Maor Ivgi, Matt Jordan, Samir Gadre, Hritik Bansal, Etash Guha, Sedrick Keh, Kushal Arora, Saurabh Garg, Rui Xin, Niklas Muennighoff, Reinhard Heckel, Jean Mercat, Mayee Chen, Suchin Gururangan, Mitchell Wortsman, Alon Albalak, Yonatan Bitton, Marianna Nezhurina, Amro Abbas, Cheng-Yu Hsieh, Dhruba Ghosh, Josh Gardner, Maciej Kilian, Hanlin Zhang, Rulin Shao, Sarah Pratt, Sunny Sanyal, Gabriel Ilharco, Giannis Daras, Kalyani Marathe, Aaron Gokaslan, Jieyu Zhang, Khyathi Chandu, Thao Nguyen, Igor Vasiljevic, Sham

Kakade, Shuran Song, Sujay Sanghavi, Fartash Faghri, Sewoong Oh, Luke Zettlemoyer, Kyle Lo, Alaaeldin El-Nouby, Hadi Pouransari, Alexander Toshev, Stephanie Wang, Dirk Groeneveld, Luca Soldaini, Pang Wei Koh, Jenia Jitsev, Thomas Kollar, Alexandros G. Dimakis, Yair Carmon, Achal Dave, Ludwig Schmidt, and Vaishaal Shankar. Datacomp-lm: In search of the next generation of training sets for language models, 2025. URL https://arxiv.org/abs/2406.11794.

Muyang Li, Yujun Lin, Zhekai Zhang, Tianle Cai, Xiuyu Li, Junxian Guo, Enze Xie, Chenlin Meng, Jun-Yan Zhu, and Song Han. Svdquant: Absorbing outliers by low-rank components for 4-bit diffusion models. *arXiv preprint arXiv:2411.05007*, 2024.

Aixin Liu, Bei Feng, Bing Xue, Bingxuan Wang, Bochao Wu, Chengda Lu, Chenggang Zhao, Chengqi Deng, Chenyu Zhang, Chong Ruan, et al. Deepseek-v3 technical report. *arXiv preprint arXiv:2412.19437*, 2024.

Paulius Micikevicius, Dusan Stosic, Neil Burgess, Marius Cornea, Pradeep Dubey, Richard Grisenthwaite, Sangwon Ha, Alexander Heinecke, Patrick Judd, John Kamalu, et al. Fp8 formats for deep learning. *arXiv preprint arXiv:2209.05433*, 2022.

Jiaqi Mu, Suma Bhat, and Pramod Viswanath. All-but-the-top: Simple and effective postprocessing for word representations. *arXiv preprint arXiv:1702.01417*, 2017.

Nvidia. Introducing nvfp4 for efficient and accurate low-precision inference — nvidia technical blog, 6 2025. URL https://developer.nvidia.com/blog/introducing-nvfp4-for-efficient-and-accurate-low-precision-inference/.

Houwen Peng, Kan Wu, Yixuan Wei, Guoshuai Zhao, Yuxiang Yang, Ze Liu, Yifan Xiong, Ziyue Yang, Bolin Ni, Jingcheng Hu, et al. Fp8-lm: Training fp8 large language models. *arXiv preprint arXiv:2310.18313*, 2023.

Sergio P Perez, Yan Zhang, James Briggs, Charlie Blake, Josh Levy-Kramer, Paul Balanca, Carlo Luschi, Stephen Barlow, and Andrew William Fitzgibbon. Training and inference of large language models using 8-bit floating point. *arXiv preprint arXiv:2309.17224*, 2023.

Giovanni Puccetti, Anna Rogers, Aleksandr Drozd, and Felice Dell'Orletta. Outliers dimensions that disrupt transformers are driven by frequency. *arXiv preprint arXiv:2205.11380*, 2022.

Alec Radford, Jeffrey Wu, Rewon Child, David Luan, Dario Amodei, Ilya Sutskever, et al. Language models are unsupervised multitask learners. *OpenAI blog*, 1(8):9, 2019.

B. D. Rouhani, A. Vincent, R. Krishnamoorthi, et al. Microscaling data formats for deep learning. *arXiv preprint arXiv:2310.10537*, oct 2023. doi: 10.48550/arXiv.2310.10537. URL https://arxiv.org/abs/2310.10537.

William Rudman and Carsten Eickhoff. Stable anisotropic regularization. *arXiv preprint arXiv:2305.19358*, 2023.

Wenqi Shao, Mengzhao Chen, Zhaoyang Zhang, Peng Xu, Lirui Zhao, Zhiqian Li, Kaipeng Zhang, Peng Gao, Yu Qiao, and Ping Luo. Omniquant: Omnidirectionally calibrated quantization for large language models. *arXiv preprint arXiv:2308.13137*, 2023.

Ananda Theertha Suresh, X Yu Felix, Sanjiv Kumar, and H Brendan McMahan. Distributed mean estimation with limited communication. In *International conference on machine learning*, pp. 3329–3337. PMLR, 2017.

Joel A Tropp. User-friendly tail bounds for sums of random matrices. *Foundations of computational mathematics*, 12(4):389–434, 2012.

Ashish Vaswani, Noam Shazeer, Niki Parmar, Jakob Uszkoreit, Llion Jones, Aidan N Gomez, Łukasz Kaiser, and Illia Polosukhin. Attention is all you need. *Advances in neural information processing systems*, 30, 2017.

Ruizhe Wang, Yeyun Gong, Xiao Liu, Guoshuai Zhao, Ziyue Yang, Baining Guo, Zhengjun Zha, and Peng Cheng. Optimizing large language model training using fp4 quantization. *arXiv preprint arXiv:2501.17116*, 2025.

Xiuying Wei, Yunchen Zhang, Yuhang Li, Xiangguo Zhang, Ruihao Gong, Jinyang Guo, and Xianglong Liu. Outlier suppression+: Accurate quantization of large language models by equivalent and optimal shifting and scaling. *arXiv preprint arXiv:2304.09145*, 2023.

Guangxuan Xiao, Ji Lin, Mickael Seznec, Hao Wu, Julien Demouth, and Song Han. Smoothquant: Accurate and efficient post-training quantization for large language models. In *International conference on machine learning*, pp. 38087–38099. PMLR, 2023.

Sangwon Yu, Jongyoon Song, Heeseung Kim, Seong-min Lee, Woo-Jong Ryu, and Sungroh Yoon. Rare tokens degenerate all tokens: Improving neural text generation via adaptive gradient gating for rare token embeddings. *arXiv preprint arXiv:2109.03127*, 2021.

Rowan Zellers, Ari Holtzman, Yonatan Bisk, Ali Farhadi, and Yejin Choi. Hellaswag: Can a machine really finish your sentence?, 2019. URL https://arxiv.org/abs/1905.07830.

APPENDIX

This section is organized to present empirical results on additional model structures and modules, which complement the *Analysis* and *Methods* sections, as well as experimental details and supplementary results that support the *Experiments* section.

A ANALYSIS

A.1 ANISOTROPY: A UNIVERSAL PROPERTY OF MODERN LLMS

The universality of anisotropy is further supported by evidence from open-sourced LLM weight matrices.

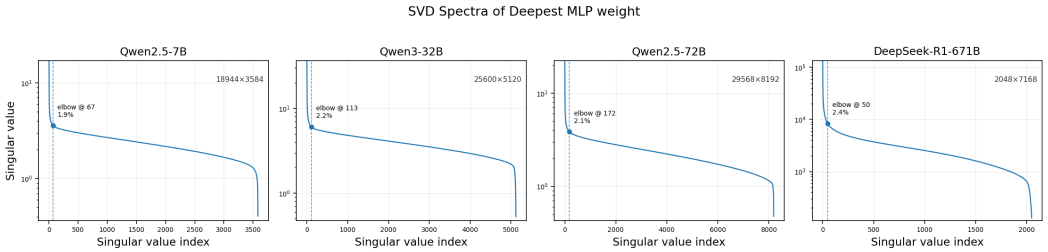

Figure 7: Singular value spectra of the final FeedForward module in Qwen2.5-7B, Qwen3-32B, Qwen2.5-72B, and DeepSeek-R1-671B. The elbow fraction $f = k^\star/r$, where $k^\star$ is the index of maximum curvature, indicates that only a small fraction of singular values dominates the spectrum (1.9%, 2.2%, 2.1%, 2.4%), demonstrating the universality of anisotropy in modern LLMs.

A.1.1 LLAMA-3 8B

Fig. 2 demonstrated that weight, activation, and gradient matrices exhibit highly anisotropic spectra, with only a few singular values carrying most of the energy. To further substantiate this observation, we provide additional results for LLaMA-3 8B in Figures below. Specifically, we show the singular value spectra and matrix distributions of W_k and W_{ffn1} from the first layer, as well as from the last layer. Consistent with the main analysis, these spectra are strongly anisotropic: the leading singular values dominate, while the majority of smaller components contribute values concentrated near zero. These results confirm that spectral anisotropy is a persistent phenomenon across different layers and parameter types.

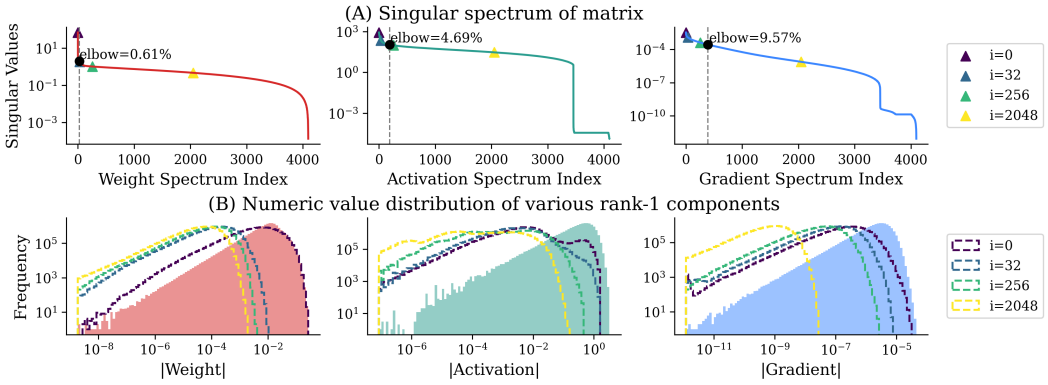

Figure 8: Analysis of weight, activation, and gradient matrices (layer 1, Attention Key). Singular value spectra show strong anisotropy, with a few values carrying most of the energy. Dominant components drive the high-value region, while smaller ones contribute near zero.

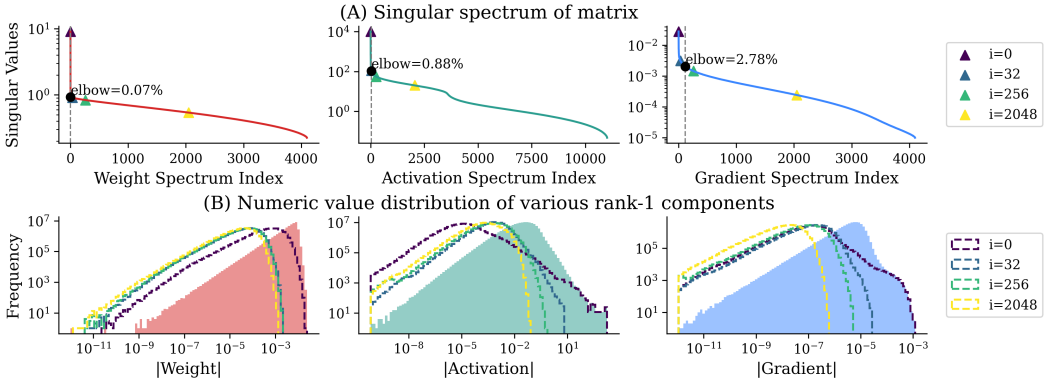

Figure 9: Analysis of weight, activation, and gradient matrices (layer 1, FFN dense2). Singular value spectra show strong anisotropy, with a few values carrying most of the energy. Dominant components drive the high-value region, while smaller ones contribute near zero.

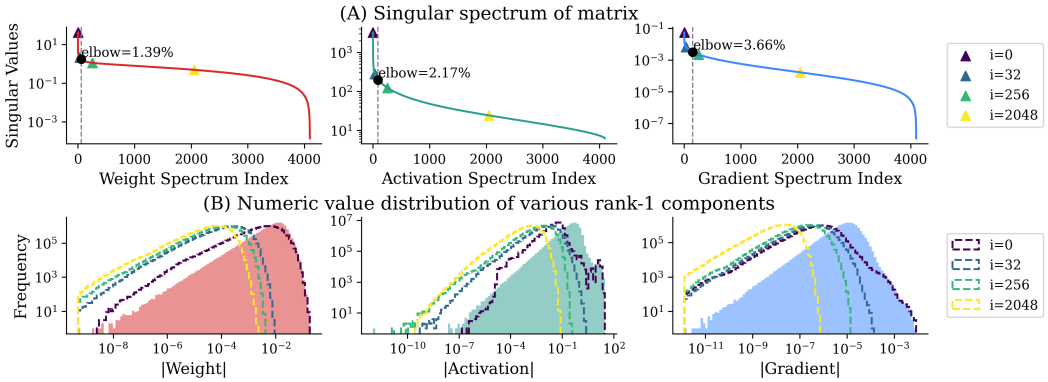

Figure 10: Analysis of weight, activation, and gradient matrices (layer 32, Attention Key). Singular value spectra show strong anisotropy, with a few values carrying most of the energy. Dominant components drive the high-value region, while smaller ones contribute near zero.

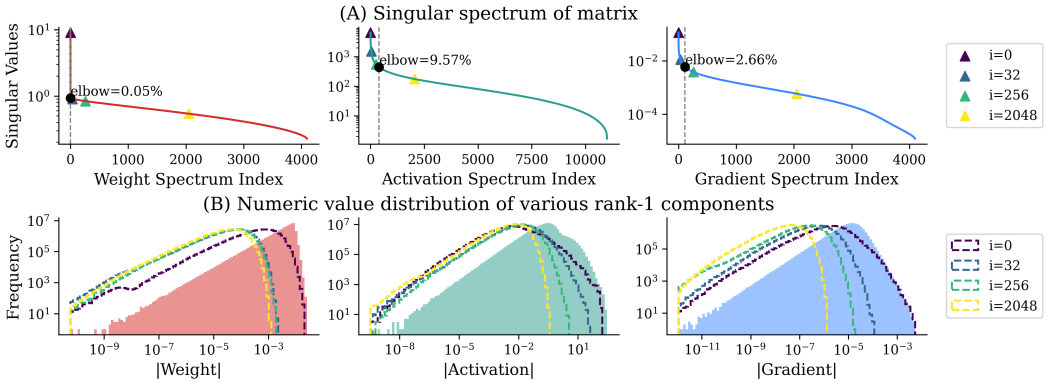

Figure 11: Analysis of weight, activation, and gradient matrices (layer 1, FFN dense2). Singular value spectra show strong anisotropy, with a few values carrying most of the energy. Dominant components drive the high-value region, while smaller ones contribute near zero.

A.1.2 GPT-2 1.1B

Fig. 2 demonstrated that weight, activation, and gradient matrices exhibit highly anisotropic spectra, with only a few singular values carrying most of the energy. To further substantiate this observation, we provide additional results for GPT-2 8B in Figures below.

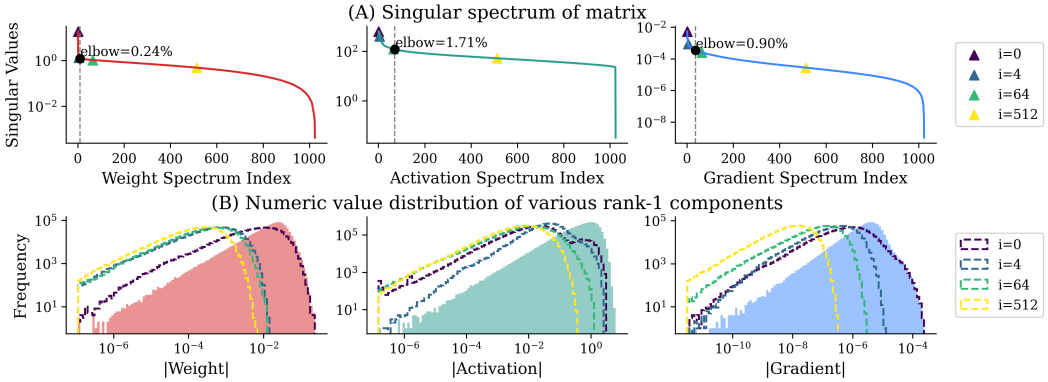

Figure 12: Analysis of weight, activation, and gradient matrices (layer 1, Attention Key). Singular value spectra show strong anisotropy, with a few values carrying most of the energy. Dominant components drive the high-value region, while smaller ones contribute near zero.

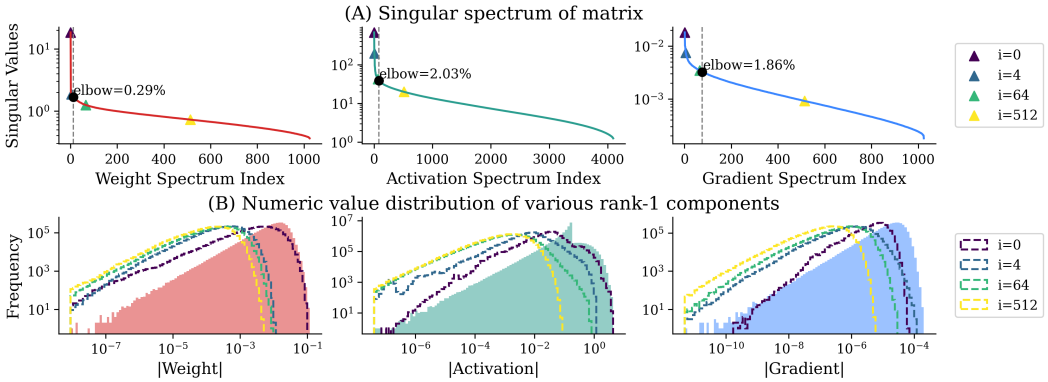

Figure 13: Analysis of weight, activation, and gradient matrices (layer 1, FFN dense2). Singular value spectra show strong anisotropy, with a few values carrying most of the energy. Dominant components drive the high-value region, while smaller ones contribute near zero.

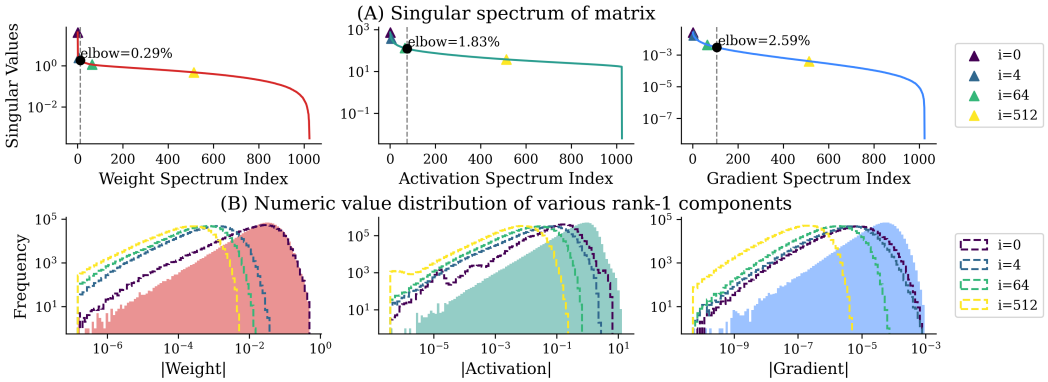

Figure 14: Analysis of weight, activation, and gradient matrices (layer 32, Attention Key). Singular value spectra show strong anisotropy, with a few values carrying most of the energy. Dominant components drive the high-value region, while smaller ones contribute near zero.

A.2 Anisotropy Induces Wide Numerical Distributions

This section provides additional empirical evidence from a broader range of models and modules, further supporting the analysis in the main text. The results demonstrate that the distributions of singular vectors remain narrow and largely scale-invariant, while the residual components are substantially compressed after removing the dominant singular values.

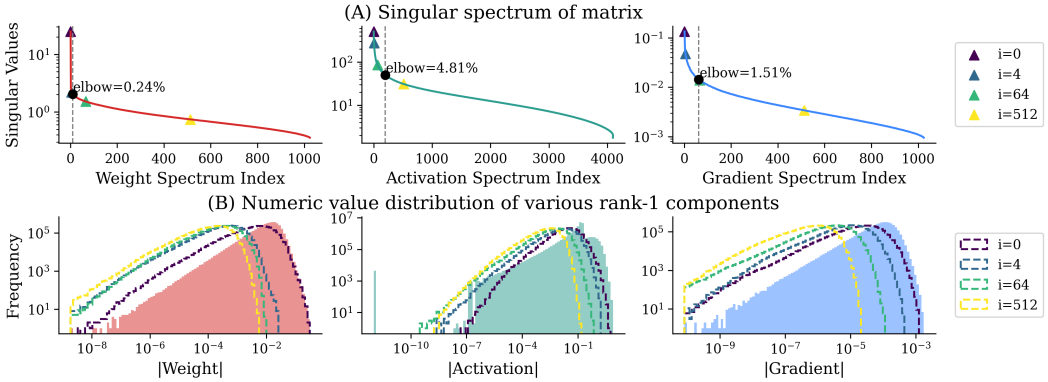

Figure 15: Analysis of weight, activation, and gradient matrices (layer 1, FFN dense2). Singular value spectra show strong anisotropy, with a few values carrying most of the energy. Dominant components drive the high-value region, while smaller ones contribute near zero.

A.2.1 LLaMA-3 8B

We include further results for LLaMA-3 8B, specifically from layer 1 and layer 32, as well as from the Key projection in the Attention module and the second dense layer in the Feed-Forward Network (FFN).

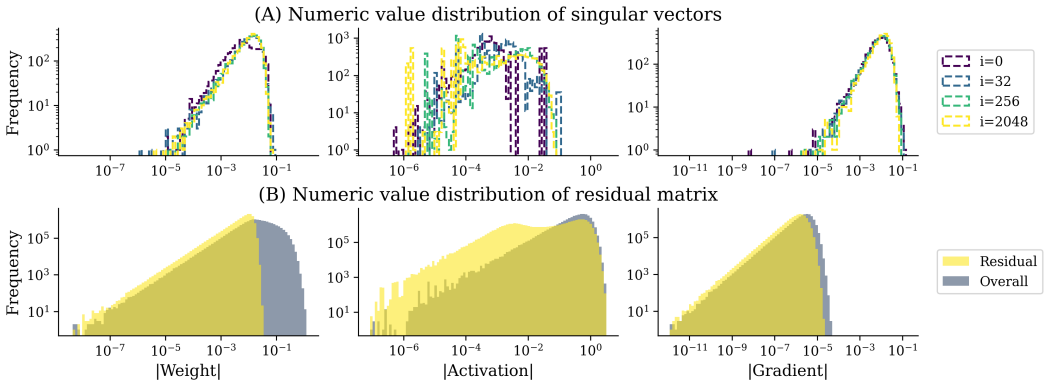

Figure 16: Analysis of weight, activation, and gradient matrices (layer 1, Attention Key), showing that singular vectors are narrow and residuals 1–2 orders of magnitude smaller, confirming wide ranges arise from dominant components amplified by large singular values.

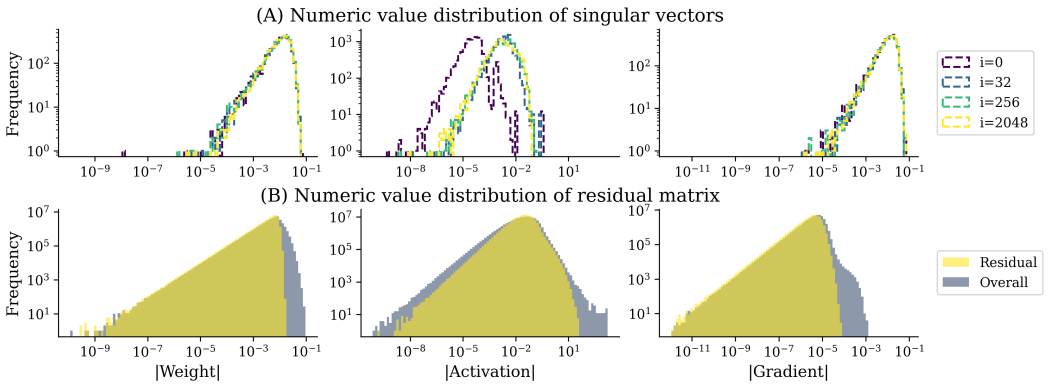

Figure 17: Analysis of weight, activation, and gradient matrices (layer 1, FFN dense2), showing that singular vectors are narrow and residuals 1–2 orders of magnitude smaller, confirming wide ranges arise from dominant components amplified by large singular values.

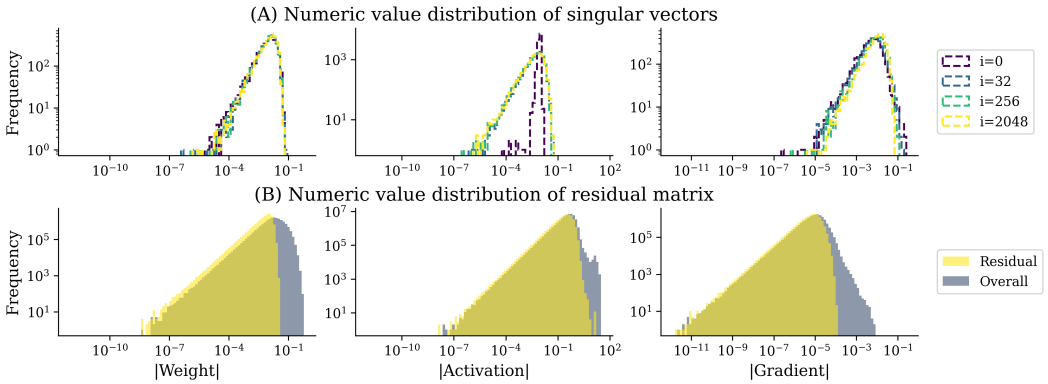

Figure 18: Analysis of weight, activation, and gradient matrices (layer 32, Attention Key), showing that singular vectors are narrow and residuals 1–2 orders of magnitude smaller, confirming wide ranges arise from dominant components amplified by large singular values.

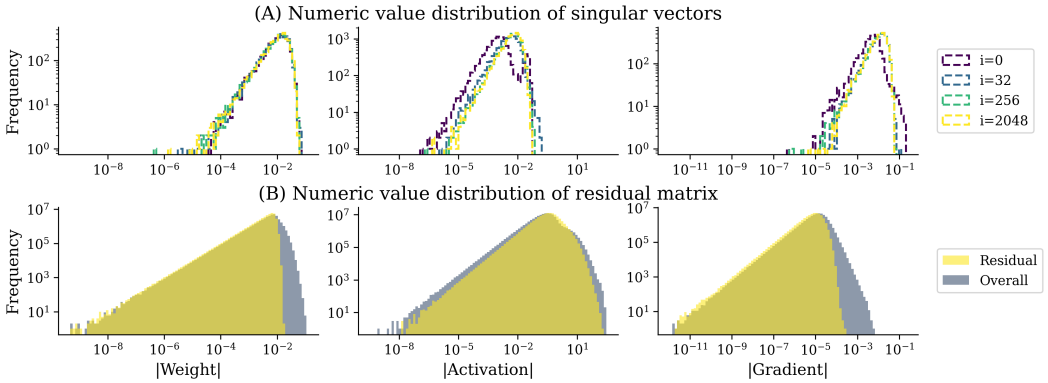

Figure 19: Analysis of weight, activation, and gradient matrices (layer 32, FFN dense2), showing that singular vectors are narrow and residuals 1–2 orders of magnitude smaller, confirming wide ranges arise from dominant components amplified by large singular values.

A.2.2 GPT-2 1.1B

We include further results for GPT-2 1.1B, specifically from layer 1 and layer 32, as well as from the Key projection in the Attention module and the second dense layer in the Feed-Forward Network (FFN).

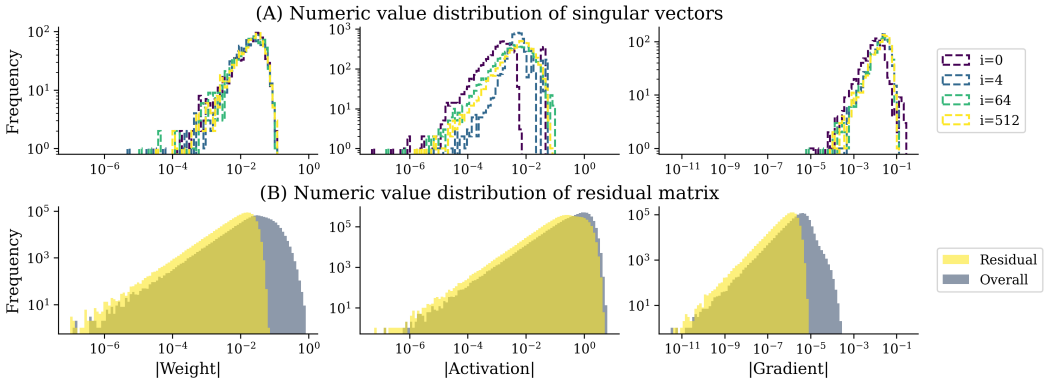

Figure 20: Analysis of weight, activation, and gradient matrices (layer 1, Attention Key), showing that singular vectors are narrow and residuals 1–2 orders of magnitude smaller, confirming wide ranges arise from dominant components amplified by large singular values.

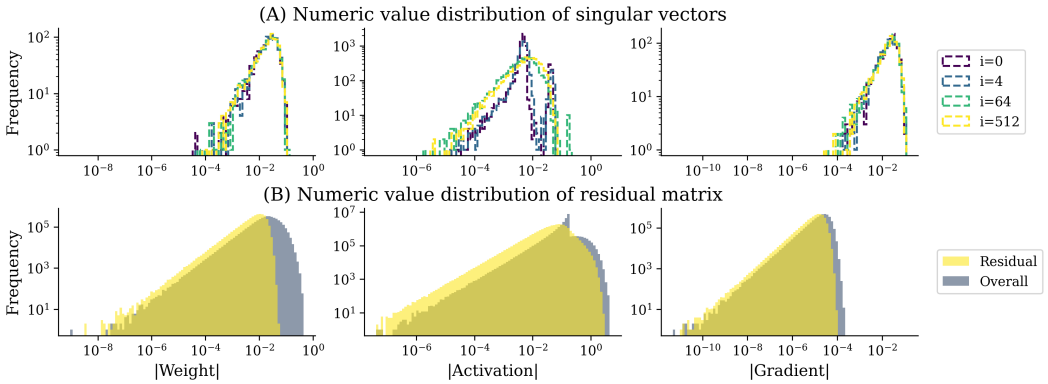

Figure 21: Analysis of weight, activation, and gradient matrices (layer 1, FFN dense2), showing that singular vectors are narrow and residuals 1–2 orders of magnitude smaller, confirming wide ranges arise from dominant components amplified by large singular values.

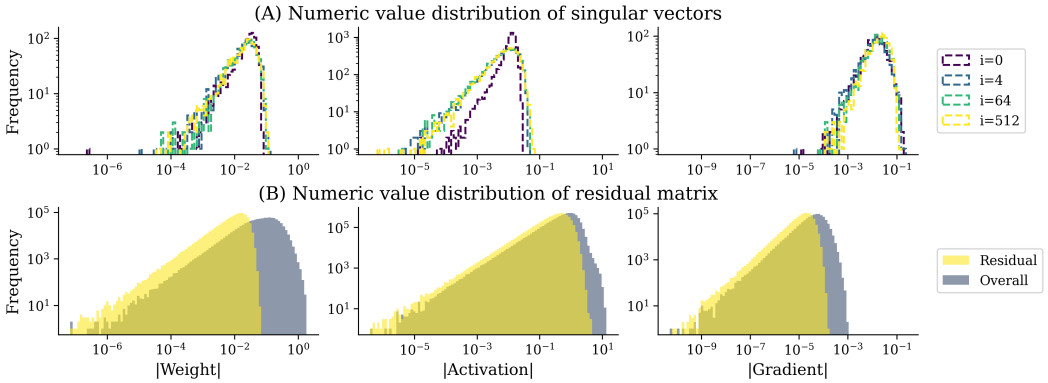

Figure 22: Analysis of weight, activation, and gradient matrices (layer 32, Attention Key), showing that singular vectors are narrow and residuals 1–2 orders of magnitude smaller, confirming wide ranges arise from dominant components amplified by large singular values.

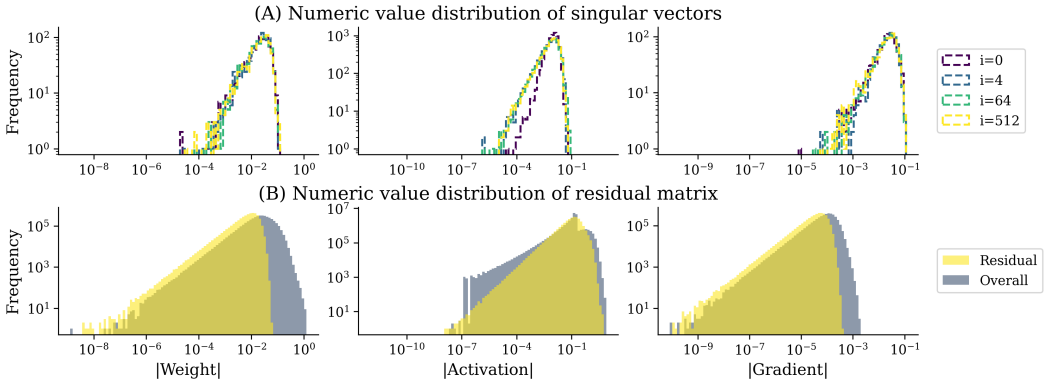

Figure 23: Analysis of weight, activation, and gradient matrices (layer 32, FFN dense2), showing that singular vectors are narrow and residuals 1–2 orders of magnitude smaller, confirming wide ranges arise from dominant components amplified by large singular values.

A.3 Numerical Distribution Comparison of Hadamard and Metis

We compare the effects of Hadamard transforms and Metis in the element space. As shown in Fig. 24, the Hadamard transform redistributes only a small fraction of outliers, modestly smoothing the tails but leaving the overall distribution wide and still misaligned with FP4's narrow representable range. In contrast, Metis applies spectral decomposition to separate dominant singular directions and values;

the residual matrix after removing these components exhibits a substantially narrower distribution, inherently more compatible with low-bit quantization.

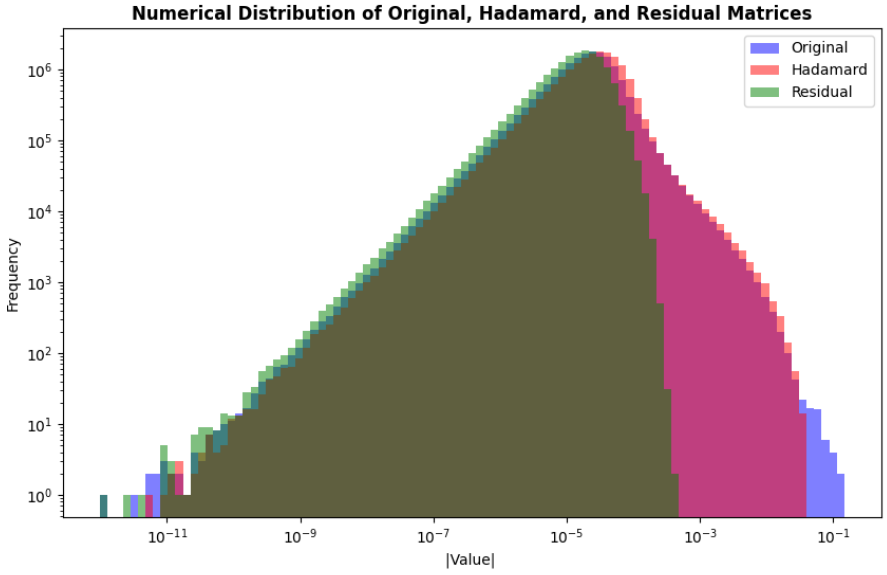

Figure 24: Element-wise distributions under different preprocessing strategies: (i) original tensor, (ii) Hadamard transform, and (iii) Metis spectral decomposition. Hadamard smooths a few outliers but leaves a wide spread, while Metis isolates dominant components and produces a narrower residual distribution well suited for FP4 quantization.

B METHOD

B.1 SPARSE RANDOM SAMPLING SUBSPACE APPROXIMATION

This section provides results on additional modules, further supporting the findings in the *Methods* section and showing that the dominant subspace of a large batch can be efficiently approximated using only a subset of samples.

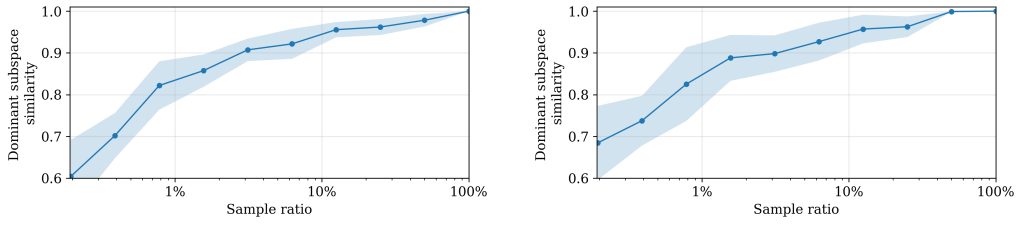

(a) (b)

Figure 25: Subspace alignment between the dominant subspace of the full batch and that of randomly sampled subsets of sequences. (a) The input activation of W_k module of layer 32. (b) The input activation of FFN module of layer 32. Alignment quickly saturates as the sample ratio increases, with just 1% of sequences achieving nearly 0.9 alignment with the full-batch subspace.

C EXPERIMENTS

C.1 IMPLEMENTATION OF NVFP4 AND NVIDIA'S RECIPE

In our implementation, the NVFP4 format is simulated by explicitly casting tensors to FP4 before invoking low-precision operators and subsequently restoring them to higher precision when passing results to subsequent high-precision operators. Concretely, the quantization function maps the scaled values of each block into the discrete representable set $\pm\{0, 0.5, 1, 1.5, 2, 3, 4, 6\}$. This process ensures that the simulated tensor values adhere to the constraints of the FP4 e2m1 format, thereby capturing the representational limitations of the hardware specification. By alternating between quantized (FP4) and restored (higher-precision) states, the simulation reproduces the effective numerical behavior of NVFP4 operators while remaining compatible with standard high-precision computational routines.

Rationale The soundness of this simulation stems from the design of FP4 hardware multiply units, which typically retain extra exponent headroom when computing intermediate products. This architectural property guarantees that low-precision multiplication does not incur overflow, even though the operands are quantized. Consequently, performing multiplications in higher precision faithfully reflects the outcome of true FP4 multipliers, since no additional rounding error or overflow is introduced in the product stage. Following the multiplication, accumulation is conducted in bfloat16 (bf16) precision, which aligns with hardware practice and preserves numerical consistency with higher-precision accumulation. Taken together, these considerations indicate that the proposed simulation of NVFP4 matrix multiplications is both practical and theoretically well-justified.

C.2 SENSITIVITY ANALYSIS OF RANK

Sensitivity analysis of spectral decomposition rank ranging from 1.5% to 12.5%. The curves for 1.5% and 12.5% closely match, indicating that a rank of 1.5% is sufficient to maintain performance.

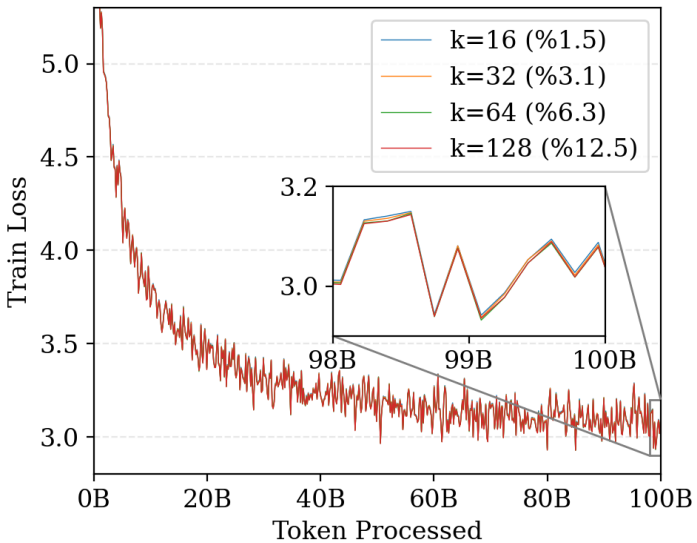

Figure 26: Training loss curves of GPT-2 1.1B using different ranks in spectral decomposition, showing that a rank of 1.5% is sufficient to maintain performance.

C.3 ISOTROPY OF THE RESIDUAL BRANCH

We inspect the singular spectrum of a residual matrix from GPT-2 trained with Metis to examine whether anisotropy re-emerges, using a baseline-trained matrix for comparison. As shown below, the baseline matrix exhibits strong anisotropy, with a few singular values dominating the spectrum, whereas the residual shows a much flatter distribution, indicating that anisotropy is effectively addressed by the low-rank branch in Metis.

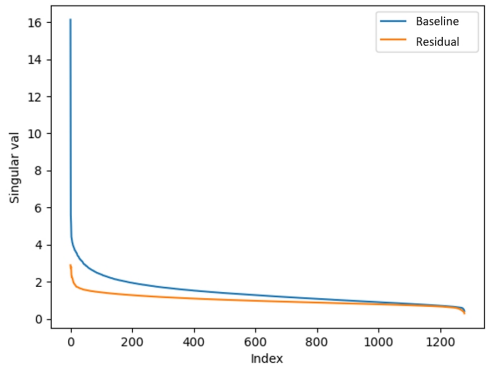

(a)

Figure 27: Inspection of residual anisotropy in Metis compared with a baseline-trained matrix (layer 16, FFN dense1, GPT-2 1.1B). While the baseline matrix exhibits strong anisotropy, the residual spectrum shows a much flatter distribution, indicating that anisotropy is effectively addressed by the low-rank branch in Metis.